International Journal of Hydrogen Energy 105 (2025) 835–844

Contents lists available at ScienceDirect

International Journal of Hydrogen Energy

journal homepage: www.elsevier.com/locate/he

X-ray measurements of gas distribution in a zero gap alkaline water electrolyzer

On-Yu Dung [a,b], Stephan Boden [d], Albertus W. Vreman [a,b,c,*], Niels G. Deen [a,b], Markus Schubert [d,e], Yali Tang [a,b]

[a] Power and Flow group, Department of Mechanical Engineering, Eindhoven University of Technology, PO Box 513, 5600 MB, Eindhoven, The Netherlands
[b] Eindhoven Institute for Renewable Energy Systems (EIRES), Eindhoven University of Technology, PO Box 513, 5600 MB, Eindhoven, The Netherlands
[c] Nobian, Van Asch van Wijckstraat 53, 3811 LP, Amersfoort, The Netherlands
[d] Institute of Fluid Dynamics, Helmholtz-Zentrum Dresden-Rossendorf, Dresden, 01328, Germany
[e] Chair of Chemical Process Engineering, Technische Universität Dresden, Dresden, 01062, Germany

ARTICLE INFO

Keywords:
Alkaline water electrolysis
X-ray
Zero gap
Gas volume fraction
Bubbles

ABSTRACT

X-ray radioscopy was used to measure the 2D projected dynamic void fraction in a zero/narrow gap alkaline water electrolyzer at a spatial resolution of 15 μm, for narrow gap sizes up to 300 μm and current densities up to 0.54 A/cm^2. As expected, the void fraction in the bulk was found to increase along the cell height and with increasing current density. The void fraction measured in the gap region (the space between the diaphragm and the electrode and its holes) was always larger than in the bulk. It hardly depended on the gap size at current densities below 0.3 A/cm^2. The lowest cell potential was measured for zero gap. No evidence of isolating gas pockets/films in the gaps was found. Liquid crossover and oxygen void fraction exceeding the hydrogen void fraction occurred for porous plate electrodes, but these phenomena were suppressed for perforated foil electrodes.

1. Introduction

Water electrolysis to generate hydrogen with renewable energy is a key technology towards a carbon-free society. Among different types of technology, alkaline water electrolysis is cost-effective and of reasonably good efficiency (see e.g. [1]). The efficiency can be further improved if ohmic losses are reduced. Zero gap between electrodes and the diaphragm is considered to minimize ohmic losses (e.g. see [2]). However, the ohmic/area resistance in zero gap cells is often found much higher than expected, i.e. much higher than the diaphragm/separator resistance [3].

It is well-known that the hydrodynamics of the electrogenerated bubbles inside the cell can affect the cell potential in nonzero gap (flat plate) electrolyzers [4]. In water electrolysis, dissolved hydrogen and oxygen gases are produced separately at the cathode and anode respectively. Upon supersaturation of the dissolved gases, H_2 and O_2 bubbles are formed [4]. Bubbles between electrodes can act as electric insulators amd lengthen the path needed for the ions to travel from one electrode to another [5], thus increasing the cell resistance while electrode coverage by bubbles can reduce the active surface area of the electrode [4]. On the other hand, as mentioned in Ref. [6], when bubbles detach from the electrode surfaces, microconvection at the boundary layer is induced, enhancing the mass transfer and thus also the cell efficiency [7,8].

In particular, for the zero-gap (or narrow gap) configuration, the origin of the high area resistance was suggested to be caused by bubbles or a gas film trapped in the gap as practically it is almost impossible to reach a true zero gap (see also [3,9–14]). It is expected that the void fraction at the gap increases with decreasing gap size. Therefore there might exist an optimal non-zero distance between the electrodes for optimal cell efficiency. For non-porous plane parallel electrodes, the optimal gap size appears to be larger than zero [9,11]. Furthermore, recently, experiments using expanded mesh electrodes were performed by Haverkort & Rajaei [13], in which a gap width of 200 μm led to a substantially lower cell voltage than a gap width of zero, suggesting that introducing a deliberate gap allows bubbles or gas films to escape more easily. For perforated plate electrodes a similar conclusion was drawn by Kienzlen *et al.* [10]. Nevertheless, the presence of gas bubbles/films in 'zero' gap still remains a hypothesis to date. To clear up the speculations in literature and the mystery of bubble/gas effects on the cell resistance in zero/narrow gap configurations, it is of primary interest to visualize and measure the gas distribution.

* Corresponding author at: Power and Flow group, Department of Mechanical Engineering, Eindhoven University of Technology, PO Box 513, 5600 MB Eindhoven, The Netherlands.
E-mail address: a.w.vreman@tue.nl (A.W. Vreman).

https://doi.org/10.1016/j.ijhydene.2025.01.110
Received 21 September 2024; Received in revised form 7 December 2024; Accepted 7 January 2025
Available online 28 January 2025

Measuring the gas distribution in electrolyzers is challenging due to opaque dense bubbly flows and the required high spatial resolution. As mentioned in Ref. [4], the attempts to measure the void fraction in which the bubbles produced by vertical plane electrodes are via image analysis (e.g. Ref. [15,16] employed high speed camera) and local intrusive probes to measure the resistivity of the bubbly electrolyte solution [15,17]. The image analysis method can yield significant error near the electrode due to bubble shadowing effect and the resistivity method assumes homogeneity of void fraction in depth [4]. In short, measuring the void fraction in narrow-gap cells poses practical challenges due to limited optical access and spatial resolution. In the past, X-ray radioscopy and tomography have been employed to study bubbly flows in porous transport layers of polymer electrolyte water electrolysis (summarized in [18]) and proton-exchange membrane water electrolysis (summarized in Ref. [19]). X-ray measurements have also been extensively employed to dense bubbly flows in many other engineering applications [20]. In this work, we only employ 2D X-ray radioscopy to measure the void fraction in an electrolyzer, including the gap region with a resolution down to 15 μm. This imaging technique utilizes the fact that X-rays penetrate an object under investigation along straight lines and refraction can be neglected for photons with energies of around 100 keV. High spatial image resolutions can be achieved if the focal spot size of the X-ray source is small. Today's microfocus X-ray sources achieve focal spot sizes of smaller than 5 μm. The attenuation of X-rays in the sample can be described by the Beer–Lambert's law whose exponent is linear to the volume fractions of the irradiated phases and materials. By employing suitable references – such as the emptied and completely filled probe to be used for two-point calibration – quantitative measurements of the phase fractions are possible. In brief, X-ray imaging is well suited for measurements in dense bubbly flows since X-rays do not undergo scattering at bubble interfaces as for visible light. To the best of our knowledge, no attempt before the current work has utilized X-ray imaging to measure the gas volume fraction in zero/narrow gap electrolyzers. The spatial resolution of this measurement technique is limited by the focal spot size and by limited magnification ratios of the projective imaging geometry, as sample sizes typically can only be reduced to a finite extent. In addition the low photon flux rates of conventional microfocus X-ray tubes mean that exposure times can only be chosen in the range of seconds, or at best of a few milliseconds, limiting the temporal resolution. Metallic internals often prevent the application of X-ray imaging techniques due to their high X-ray attenuation. In order to prevent calibration errors it is also important to ensure that the object to be investigated has a high mechanical stability without the reference structures shifting between the individual reference and test measurements.

Another phenomenon that will be addressed in this paper is the liquid crossover through the diaphragm. Liquid crossover is a cause of dissolved gas crossover. Gas crossover has become an ongoing industrial challenge due to the resulted risk in safety and the gas purity. Some research on this phenomenon is available in open literature [21–24]. One transport mechanism is through the electro-osmotic flow induced by the electric potential difference across the diaphragm, which is observed in Ref. [25,26]. In this work, we try to determine and understand the crossover in a zero-gap cell using electrodes with different porosity and surface wettability.

The experimental setup and method is elaborated in Section 2. Then, the overall structure of the bubbly flows and the typical current–voltage curve are illustrated in Section 3.1. After that, the effect of gap size and current densities on the measured void fraction are uncovered quantitatively in Section 3.2. This is followed by a further analysis on the gas contribution to the cell voltage in Section 3.3. In Section 3.4 the crossover phenomenon is addressed by comparing the different hydrodynamic behaviors in zero-gap configurations using two different electrodes.

2. Experimental setup and methods

2.1. In-house built cell

A cell was built that fitted into the X-ray scanner. Fig. 1a shows the details of the cell design. The electrodes are perforated nickel plates with thickness 0.5 mm unless otherwise specified. The active dimensions of each electrode are 9.4 cm in height × 0.96 cm in width, which give the apparent area of 9.0 cm^2. It has a porosity of 0.5 (see Fig. 10a for the technical drawing). We employed Agfa's Zirfon PERL UTP 500 diaphragm (500 μm thick) [27]. To create a gap between the separator and the electrodes, we use spacers (PEEK) with a thickness of 50 μm or 100 μm, which allows for adjustable gap sizes between 0 to 300 μm. The spacers can be placed either between the electrodes and the diaphragm or outside the electrodes (see Fig. 1b).

Lastly, throughout this study, the electrolyte used is potassium hydroxide (KOH) solution with an initial concentration of 24 wt% KOH and an initial temperature around room temperature before starting a series of electrolysis experiments (elaborated below). The experiments were performed under ambient pressure.

2.2. X-ray radioscopy measurement and the cell voltage measurement

We employed X-ray radioscopy to measure the void fraction in the in-house built electrolyzer. Fig. 1d shows the details of the X-ray setup in this work and Fig. 1e shows a picture of the setup in operation. For the X-ray radioscopy system, we employed a two-dimensional flat panel X-ray image detector (PerkinElmer XRD 0822 AP3 IND; 205 × 205 mm^2 total active area covered by 1024 × 1024 pixels) and a microfocus X-ray tube (XrayWORX XWT - 190 - TC) [28].

The X-ray source is practically a point source with a focal spot size of less than 5 μm and generates an X-ray cone beam. The distance between the X-ray source and the centre of the electrolyzer was 30 mm. The distance to the X-ray detector was choosen to be 400 mm such that each detector pixel covers an beam cross-section of roughly 15 × 15 μm^2 in the center of the electrolyzer. Thus, the detector covers roughly 15 mm of the height of the electrolyzer. The exposure time of the detector was set to 200 ms at the beginning of each radioscopic scan and was set to 600 ms further on. The frame rate is the inverse of the exposure time, i.e. 5 fps and 1.67 fps respectively.

To create an electric potential difference between the electrodes, they are connected to a direct current power supply (KORAD, KA3005P) with a setup accuracy of $\leq 0.5\% + 10$ mA current with ripple current ≤ 3 mA_{rms} operated in constant current mode. For the cell voltage measurement, we measure the voltage across the electrodes by a National Instrument data acquisition module (NI-9215, 16 bit, ±10 V range with 0.02 percentage error) that converts the analogue voltage signal to a digital signal. The acquisition rate is 100 Hz.

2.3. Experimental procedure and image analysis

Fig. 2 gives an overview of the experimental procedures and the X-ray image analysis leading to the void fraction. The raw X-ray projection images are preprocessed in such way that the detector's dark current signal firstly is subtracted and then the signals of defective pixels are replaced by average signals from neighboring non-defective pixels (see Section 3.2 in Ref. [28]). Basically, the detectors signals linearly represent the local intensity $I(x, y)$ of the impinging X-ray beam in the detector plane with (x, y) representing the 2D location of the pixels in the detector plane.

We define the attenuation by $A = -\ln(I/I_0)$, where I_0 is the intensity of an X-ray beam emitted from the source and I is the measured intensity of the X-ray beam after passing through the material between the source and the detector. The coordinate system (x, y) is specified in Fig. 3 which is parallel to the detector plate. Denote t as the time coordinate. We define the attenuations $A_{empty}(x, y)$, $A_{full}(x, y, t)$,

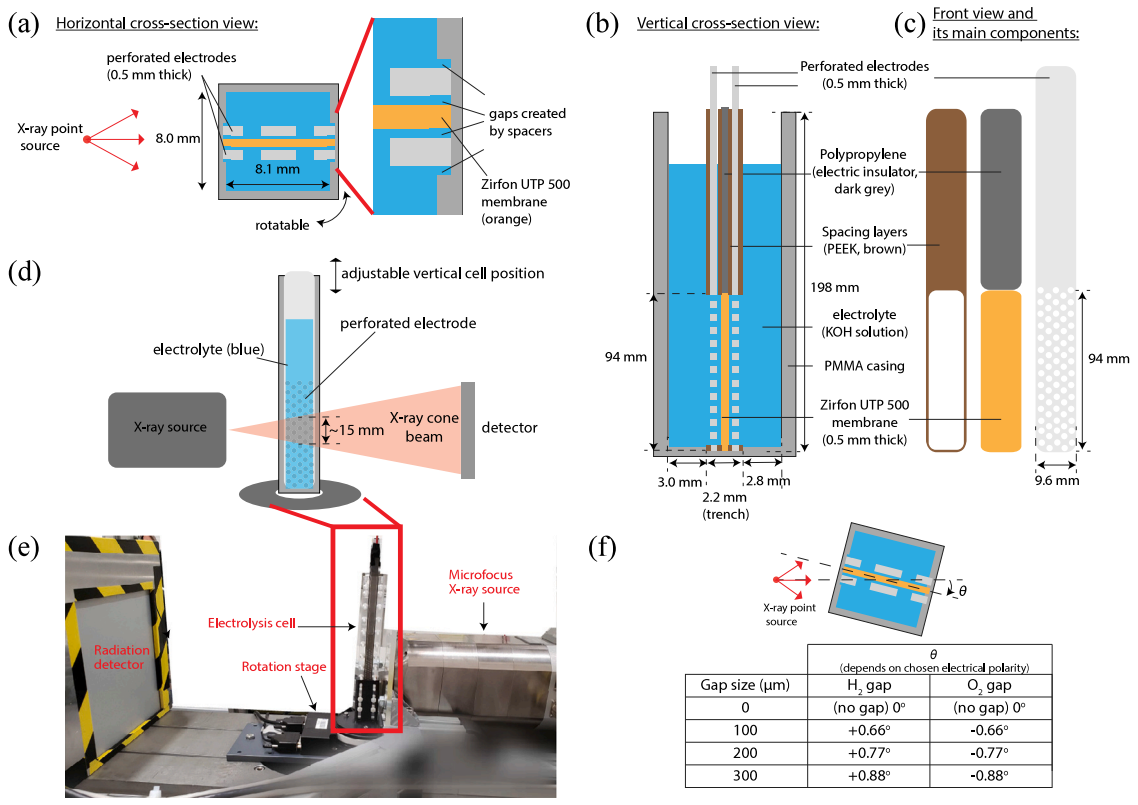

	θ (depends on chosen electrical polarity)	
Gap size (μm)	H_2 gap	O_2 gap
0	(no gap) 0°	(no gap) 0°
100	+0.66°	-0.66°
200	+0.77°	-0.77°
300	+0.88°	-0.88°

Fig. 1. (a) Horizontal cross-section, (b) vertical cross-section and (c) front view of the in-house built electrolyzer including the compositions and the corresponding dimensions. (d) Schematics of the setup for the X-ray radioscopy. (e) The setup for X-ray radioscopy. (f) The cell rotation angle (anti-clockwise positive) for different gap sizes and gaps (H_2 or O_2). The angle was chosen such that the vector parallel to the membrane center (inclined dashed line) but through the center of the gap pointed towards the X-ray source point.

and $A_{exp}(x, y, t)$ as the attenuation measured when the electrolyzer has no electrolyte (except in the diaphragm) which is stationary, when the electrolyzer is full of electrolyte (no current), and during an electrolysis experiment, respectively. By Beer–Lambert's law, A increases linearly with the thickness of a material an X-ray beam has passed through. This implies the liquid volume fraction $\alpha_L = (A_{exp} - A_{empty})/(A_{full} - A_{empty})$, and the void fraction

$$\alpha(x, y, t) = 1 - \alpha_L(x, y, t) = 1 - \frac{A_{exp}(x, y, t) - A_{empty}(x, y)}{A_{full}(x, y, t) - A_{empty}(x, y)}. \quad (1)$$

For each series of electrolysis experiments (see Fig. 2a for the whole experimental procedure), the cell's vertical position in the X-ray beam was fixed, and each scan focused at the H_2/O_2 gap or at the center of the separator for the zero-gap case (see Fig. 1f for the angles rotated for different gap sizes and gaps). The main experimental procedures were as follows: (1) scanning the empty cell to obtain $A_{empty}(x, y)$ averaged over the measurement time; (2) scanning of the cell filled with electrolyte ($A_{full,i}(x, y, t)$), where i denotes the ith electrolysis experiment and $i = 0$ denotes the initial 'full' case; and scanning of the cell at a current density j.

Note that in between two electrolysis experiments, if we observed any liquid level drop, fresh electrolyte was refilled to maintain a consistent initial level for all electrolysis experiments for each series of measurements. In addition, the chemical reactions resulted in a net consumption of H_2O and a time-dependent density of the electrolyte. This implies that $A_{full} - A_{empty}$ is changing over time. Thus, we established a time dependent scaling factor to account for this dynamic change of electrolyte density in the determination of void fraction (see Appendix A for details (supplementary data)). For the whole procedure on obtaining the void fraction from X-ray raw images, we refer to Fig. 2b.

Because of the 2D nature of X-ray radioscopy, the gap region is defined as the thin rectangular zone between the diaphragm on one side and the electrode and its perforations on the other side. The void fraction in the gap region is then the 2D projection of the 3D void fraction in this region, such that each point of the 2D projection represents an average along a line starting from the point source of the X-ray beam. Therefore, the 2D projection gives the void fraction

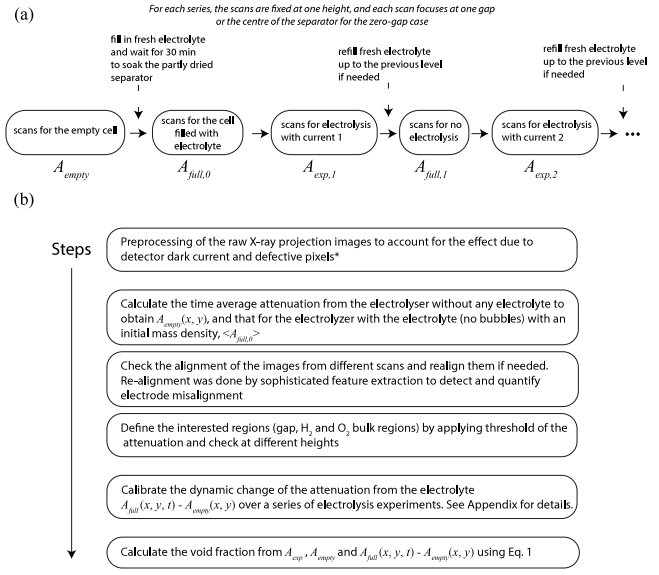

Fig. 2. (a) Experimental procedure of a series of electrolysis experiments with the scans and actions performed. Below each step, the corresponding attenuation of the X-ray is obtained. (b) Procedures for obtaining the void fraction from the raw X-ray images. *For details, we refer to the first paragraph of Section 3.2 (except the tilting part) in [28].

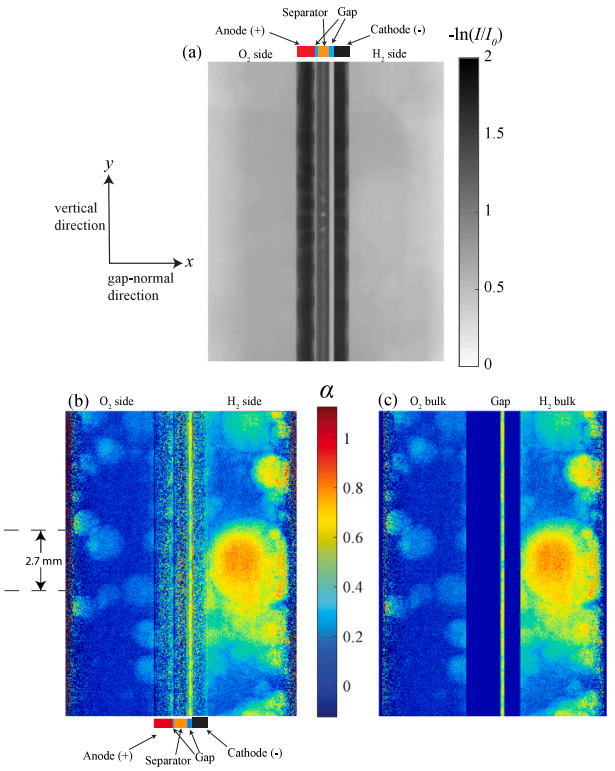

Fig. 3. (a) Snapshot of the attenuation $-\ln(I/I_0)$ from radiography for the current density $j = 0.16$ A cm^{-2}, gap size $l_d = 200\,\mu$m, KOH concentration 24 wt%, centering at height $H = 60$ mm, and focusing at the H_2 gap (i.e. a side view). (b) The corresponding instantaneous void fraction α (Eq. (1)) for the attenuation image without applying a mask. (c) The corresponding instantaneous void fraction α for the attenuation image after applying a mask.

averaged over the whole penetration depth through the cell along its thickness perpendicular to the image plane (see Fig. 1a and d).

An example of the attenuation image of an electrolysis experiment and the corresponding void fraction distribution is shown in Fig. 3, obtained from the attenuation profile (Fig. 3a), with the void fraction profile from two-point calibration (Fig. 3b), and finally with masks applied (Fig. 3c). There are artefacts near the electrodes (nonphysical red patches and lines), which resulted from the misalignment between reference and electrolysis measurement due to electrode motion. Similarly, the shapes of screws and horizontal streaks which are the boundary of the cell holder can be observed in the radiographs (see Fig. 5). The signal noise is due to the inherent randomness of the generation and interaction of X-ray photons, and is more pronounced in regions of small penetration depth at the vertical image edges or in regions of strong attenuation in the references. We refer to Appendix A for the details of the masking and the determination of the void fraction in the gap region (supplementary data).

Note that the current measurements do not distinguish between H_2 and O_2 gases for the void fraction. In Section 3.4 and Appendix C (Supplementary data), we quantify the effect of the liquid cross-over which might drive the diffused gases from one chamber to another.

3. Results

The parameter space is spanned by different gap sizes l_{gap}, vertical cell positions in the X-ray beam H, and current densities j. For each pair of l_{gap} and H, we performed electrolysis experiments for $j = \{0.01, 0.16, 0.27, 0.48, 0.54\}$ A/cm^2. To investigate the height dependence, we fixed $l_{gap} = 200\,\mu$m and varied $H = \{28, 44, 60, 76\}$ mm, while keeping in mind the total height of the active electrode is 94 mm.

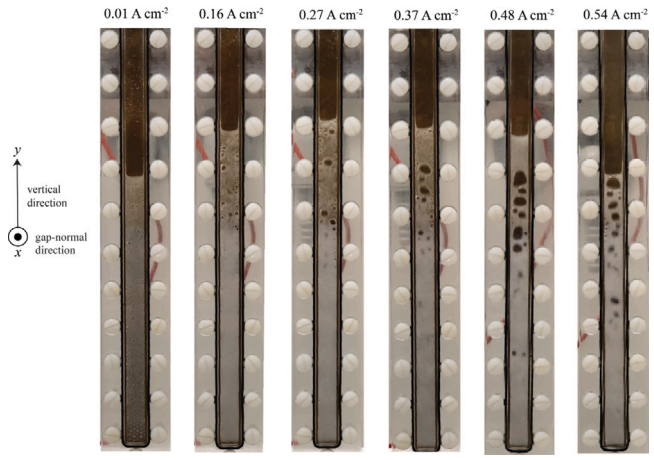

Fig. 4. Snapshots of the front view of the bubbly flows of the electrolyzer for different current densities (increasing to the right) and for a gap size of 100 μm. The snapshots here are only for reference with no indication of which chamber is referring to (the four cases from the left have the same chamber facing the camera and the two cases from the right have the same). We refer to the Supplementary data for the corresponding videos.

To investigate the gap size dependence and unless otherwise specified, we fixed $H = 60$ mm and varied $l_{gap} = \{0, 100, 200, 300\}$ μm. The initial KOH concentration for each series of electrolysis measurements (fixed l_{gap} and H but varying j) is 24 wt%. For the statistical notation, unless otherwise specified, we use a bracket $\langle\alpha\rangle$ as the spatial average and an upper bar $\overline{\alpha}$ as the time average.

3.1. The overall structure of the bubbly flows, typical void fraction dynamics and typical IV curves

The overall structures of the bubbly flows are qualitatively examined. The snapshots of the bubbly flows of the whole electrolyzer from current densities ranging from $j = 0.01$ A cm^{-2} to $j = 0.54$ 1 A cm^{-2} are shown in Fig. 4. As expected, the bubbly flow gets denser as more gas is produced with increasing current density. One interesting observation is that coalescence clearly occurs in our experiments, especially at the upper part of the cell. The coalescence results in big bubbles, or even plugs at current density higher than 0.48 A/cm^2. This might be due to the geometrical dimensions of the cell. Moreover, the void fraction seems to increase over the cell height, which provides an indication what to expect from the X-ray measurements presented in the next section. We note that the structures of the bubbly flows are different for different current densities Fig. 5). The structures and liquid level are relatively unsteady for high current densities (see the videos related to Fig. 5 in the Supplementary data).

Fig. 5 shows examples of instantaneous void fraction profiles, time-averaged 2D void fraction profiles spanning over height of ±2.7 mm around the middle of the scan, and time trajectories of the spatially-averaged void fraction $\langle\alpha\rangle$ over the mentioned region at different current densities. We perform the averages over such region to exclude artefacts mentioned in Section 2.3. The movies of such radioscopy scans are provided in the Supplementary data. We distinguish between the gap region (the radiography focuses at the O_2 gap in Fig. 5), the hydrogen (H_2) bulk region and the oxygen (O_2) bulk region. For α measured in the gap region, denoted as α_{gap}, we emphasize that it is obtained by inferring the projections of the regions not only between the separator and the electrode material but also the region which faces the holes of the electrode (see Fig. 1a), meaning that we include the gas also facing the holes but also facing the electrode material (i.e. not the true void fraction between the electrode material and the separator). The spatial average $\langle\alpha_{gap}\rangle$ has an absolute error of ±5% due to the possible movement of the electrolyzer during the scan. The explanation

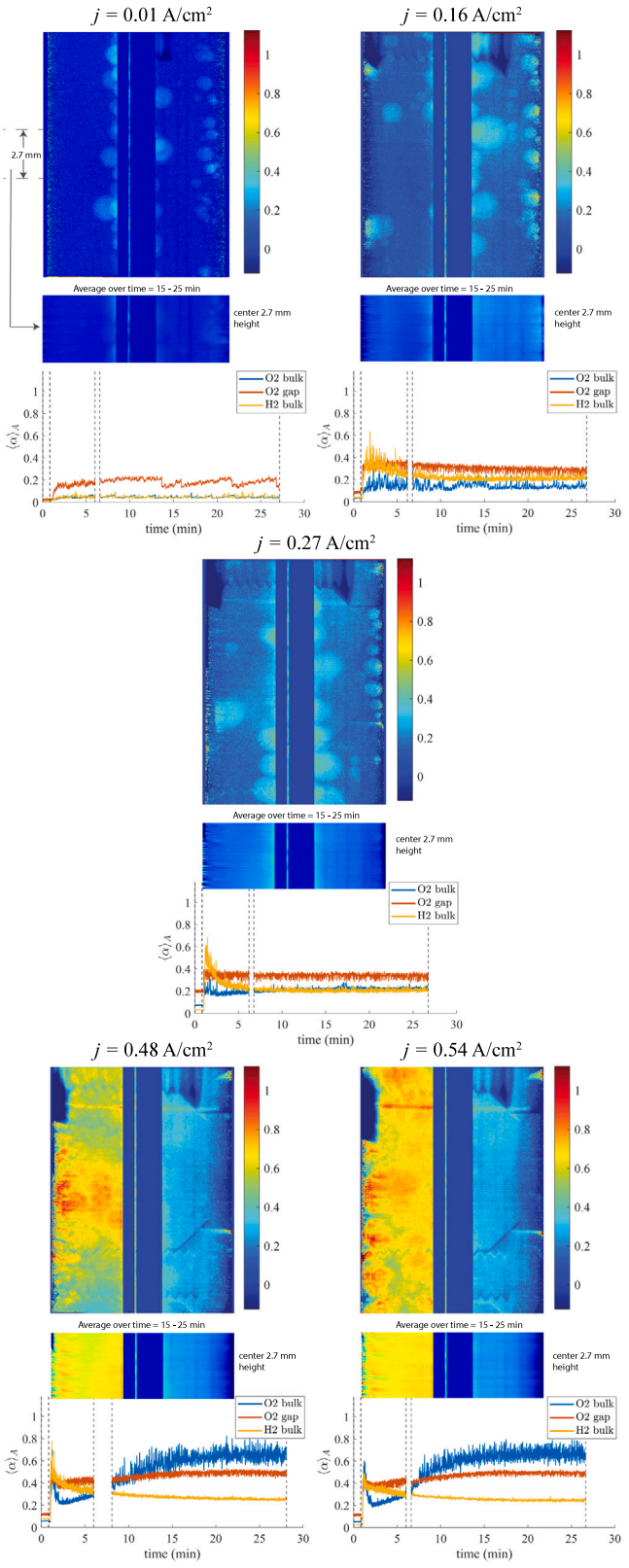

Fig. 5. Spatially averaged void fractions $\langle\alpha\rangle$ versus time t for different current densities j with the corresponding snapshots at around t = 17 min and the time averaged 2D profile at the center 2.7 mm height. The radioscopy for this set of measurements focuses at the oxygen (O_2) gap and the gap size is 100 μm (i.e. side view). The spatial average of α is taken over ±1.4 mm from the mid-height of the image, as indicated next to the j = 0.01 A/cm² image. The shape of a screw and the horizontal streaks are visible at the top and the bottom of the radioscopy images. See the Supplementary data for more explanation and for the videos.

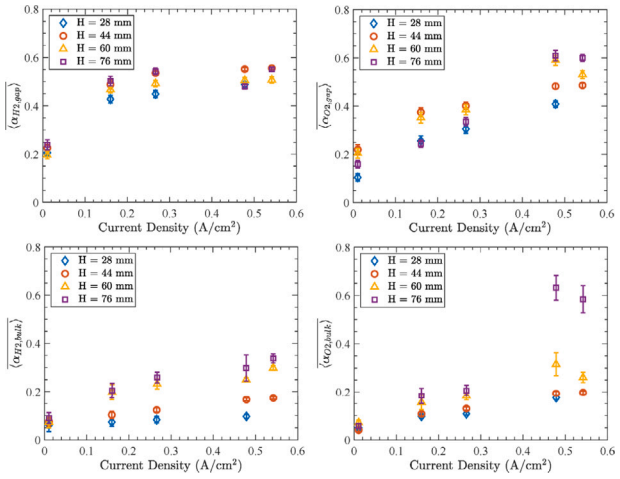

Fig. 6. Mean void fractions at H_2 gap ($\overline{\langle\alpha_{H2,gap}\rangle}$), O_2 gap ($\overline{\langle\alpha_{O2,gap}\rangle}$), H_2 bulk region ($\overline{\langle\alpha_{H2,bulk}\rangle}$) and O_2 bulk region ($\overline{\langle\alpha_{O2,bulk}\rangle}$) vs. current density at different heights of the cell with a gap size l_{gap} = 200 μm. Multiple realizations for the same gap and same current densities are averaged. The error bars represent the propagated errors from individual standard deviations of the spatial averaged void fraction over time. For $\overline{\langle\alpha_{H2,gap}\rangle}$ and $\overline{\langle\alpha_{O2,gap}\rangle}$, the absolute error is ±5% due to the possible movement of the electrolyzer during the scan (see Appendix A for explanation (Supplementary data)).

of this absolute error and the calculation of α_{gap} and its statistics are given in Appendix A (Supplementary data).

When the current density increases, we expect more gas to be produced per unit time because of higher rate of the electrochemical reactions. The typical snapshots and time series of the void fraction in Fig. 5 show that the void fraction indeed increases with increasing current density. Growing bubbles are observed at the cell walls. This can be due to the PMMA surface wetting properties (a water droplet contact angle of 68° [29]) which may promote bubbles sticking at the wall. Another observation from the void fraction time series is that, except for the lowest current density j = 0.01 A cm^{-2}, there is a build up of the void fraction after turning on the current, which is characterized by a sudden rise to a peak and a subsequent decay.

The measured void fraction at the gap reaches a steady value within 10 min at all investigated current densities. However this is not the case for the void fractions at the bulk. At $j \leq 0.27$ A/cm², both the H_2 and O_2 bulk void fractions become steady within 10 min, and their ratio is close to the stoichiometrics of the hydrogen evolution reaction (HER) and the oxygen evolution reaction (OER). At higher current densities (j = 0.48 A/cm² and 0.54 A/cm²), there is a crossing behavior of these two bulk void fractions, i.e. the O_2 bulk fraction keeps increasing and H_2 bulk fraction keeps decreasing, resulting in a much higher void fraction in the O_2 chamber than that in the H_2 chamber. This behavior is interesting and will be further elaborated in Section 3.4.

Moreover, at high current densities we observe that the instantaneous void fraction sometimes exceeds the maximal spherical packing fraction (0.74). This is due to the significantly large bubble size (approaching to plug flow) and sometimes their sticking behavior to the wall (see Supplementary data).

3.2. Effect of gap size, current density and height dependence on void fraction

This section characterizes quantitatively the dependence of the void fraction on the gap size, the cell height, and the current density. Before reporting the results, we would like to make few remarks on the data analysis for proper interpretation of the results.

First, each scan is conducted with a focus at either H_2 gap, O_2 gap or the center of the membrane (for zero-gap case); $\alpha_{H2,bulk}$ and $\alpha_{O2,bulk}$ can be measured by focusing on any of these regions, and the results

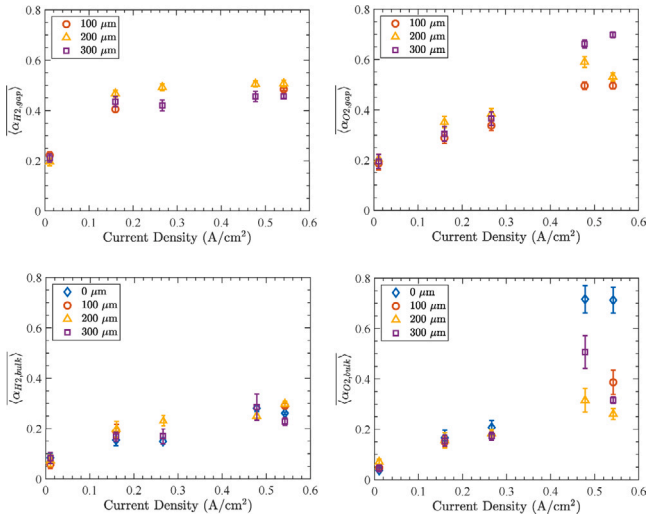

Fig. 7. Mean void fractions at H_2 gap, O_2 gap, H_2 bulk region and O_2 bulk region (symbols same as Fig. 6) vs. current density at $H = 60$ mm of a cell with different gap configurations.

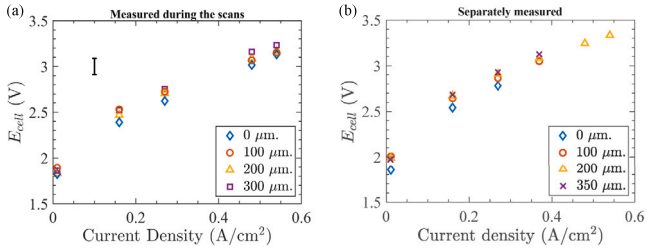

Fig. 8. The mean cell voltage E_{cell} vs. current density for different gap sizes for the experiments performed (a) during the CT and radiography scans, and (b) at a different occasion but similar temperature for each current density. For (a), each symbol is an average of different realizations for a given current density and given gap size, and the temperature for each realization is not precisely known, in contrast to (b) which each data point is obtained only through one realization and the temperature only depends on the current density but not the gap size. The error bar in (a) of ±0.1 V denotes the average spread of the mean cell voltages for different realizations. For each cell voltage measurement, the standard deviation of the voltage time series is of $\mathcal{O}(0.01\,\mathrm{V})$ which is smaller than the marker size, thus not shown in the plot.

between focusing at the two gaps are similar in an electrolysis experiment (not shown here). Therefore, in our analysis, we use the $\alpha_{H2,bulk}$ and $\alpha_{O2,bulk}$ values obtained by focusing at the H_2 gap or the center of the membrane (for zero-gap case). Time averaging is performed for the void fraction data during the last 10 min of the electrolysis experiment, where statistical equilibrium is achieved for $j \leq 0.27$ A/cm^2, except for $j = 0.01$ A/cm^2 in which the average starts from 5 min after turning on the current. We note that for $j \geq 0.48$ A/cm^2, statistical equilibrium is *not* always achieved. As mentioned in the previous section, for $\alpha_{H2,gap}$ and $\alpha_{O2,gap}$, the absolute error is ±5% due to the misalignment of the electrolyzer during the scan (see Appendix A for details (Supplementary data)).

Fig. 6 shows the mean void fractions at different heights along the cell with a gap size of 200 μm for different current densities. Overall, the void fraction at the gaps is consistent along the cell height. In contrast, the void fractions at the bulk show a clear height dependency, namely the gas holdup increases along the height as bubbles flow upwards. Despite some uncertainties in the data acquired at high current densities (as discussed in Section 3.1), these observations agree with the expectations. With regard to the dependency on current density, the overall void fraction in the cell increases with increasing density except for the void fraction at the H_2 gap; $\alpha_{H2,gap}$ quickly reaches a plateau of around 0.5.

The mean void fraction $\overline{\langle\alpha\rangle}$ (time average of $\langle\alpha\rangle$) versus current densities for different gap sizes at a cell height $H = 60$ mm is shown in Fig. 7. Similar dependency on the current density can be seen in this figure as well. If excluding the data at the bulk at high current densities (due to uncertainties discussed earlier), we do not see a clear gap size dependency of the void fraction in the cell.

3.3. Effect of gap size and bubbles on cell voltage

The mean cell voltage E_{cell} vs. current density for different gap sizes are shown in Fig. 8. Fig. 8a show the results measured during the X-ray scanning experiments. It should be noted that the temperature per test might vary since there is no temperature control of the setup. The results in this plot are reported as an average of three experimental realizations under each operating combination of j and l_{gap}. As shown by the error bars, there exists a relatively large standard deviation (0.2 V), which is mainly due to temperature differences among different realizations. Therefore, to make a valid comparison, we performed the cell voltage experiments separately at a different occasion without the radiography scans but now with similar temperature for each j and different l_{gap}, as shown in Fig. 8b, in which each data point is obtained only through one realization. For each cell voltage measurement, the standard deviation of the voltage time series is of $\mathcal{O}(0.01\,\mathrm{V})$, which is smaller than the marker size thus not shown in the plot.

These results show that the zero gap case is the most efficient, although only slightly. This observation differs from the findings in Ref. [13] where the best performance was found with a gap distance of 200 μm, possibly via stimulating bubble escape from the gap. We assume that these different findings are attributed to the cell configuration. For the cell built in Ref. [13], bolts tightening is applied to electrode and membrane, whereas in our cell only bolts tightening the cell are used to seal the O-ring for leakage prevention. In our zero-gap case, membrane and electrodes are just placed directly next to each other without being squeezed by bolts. This leads to different compression of the cell, which has been shown in Ref. [2] to influence the cell voltage.

From the CT scan, we conclude that the gap (if existing) between the diaphragm and electrode for our zero-gap case is not larger than the spatial resolution of 15 μm. We cannot absolutely disregard the possibility that there is a small amount of electrolyte between the electrodes and the diaphragm below even in the zero gap case and possible replenishment with the bulk electrolyte over time.

Furthermore, we try to quantify the contribution of gas/bubbles to the cell resistance in our measurements. First, Ohm's law is applied to determine the voltage drop across the gap, which is given by

$$|j| = \lambda \frac{E_{gap}}{l_{gap}}, \tag{2}$$

where j is the current density, λ is the effective conductivity of the bubbly electrolyte solution in the gap, E_{gap} is the potential drop across the gap and l_{gap} is the width of the gap. Both, H_2 gap and O_2 gap contribute to the total cell potential drop which is given by,

$$E_{gap,\mathrm{total}} = E_{gap,\mathrm{H_2}} + E_{gap,\mathrm{O_2}}. \tag{3}$$

The estimation of the effective conductivity in Eq. (2) follows the Bruggeman's model $\lambda_i = \kappa(1 - \overline{\langle\alpha_{i,gap}\rangle})^{3/2}$, where κ is the conductivity of the electrolyte [5], see Appendix B for more details (Supplementary data). By applying $\overline{\langle\alpha_{i,gap}\rangle}$ with a zero value or the measured value as shown in Fig. 7, we obtain $E_{gap}(0)$ and $E_{gap}(\overline{\langle\alpha_{i,gap}\rangle})$, which considers the pure electrolyte and the bubbly electrolyte, respectively. The difference corresponds to the contribution of bubbles to the cell potential drop

$$E_{gap,bub} \equiv E_{gap}(\overline{\langle\alpha_{i,gap}\rangle}) - E_{gap}(0) \tag{4}$$

The results are shown in Fig. 9. As shown in the figure, $E_{gap,bub}$ increases with the current density, as a result of the increasing void fraction.

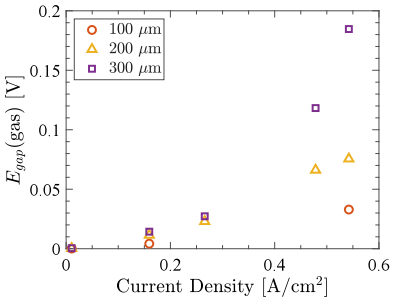

Fig. 9. Estimated cell potential drop due to presence of gas/bubbles at the gap for different gap configurations at different current densities (see Eq. (4) for the definition).

Table 1
Properties of the electrodes used in this study.

Electrode type	Liquid contact angle[a]	Porosity	Thickness (mm)
Nickel plate	11° to 65° [30]	0.4	0.5
Nickel foil-PMMA	67.8° (for PMMA) [29]	0.08 ± 0.01[b]	$0.5 + \mathcal{O}(0.1)$

[a] Refers to the side facing the bulk region at the chamber.

[b] The uncertainty is due to the uncertainty from the hole size (the diameter is between 0.1 mm to 0.12 mm).

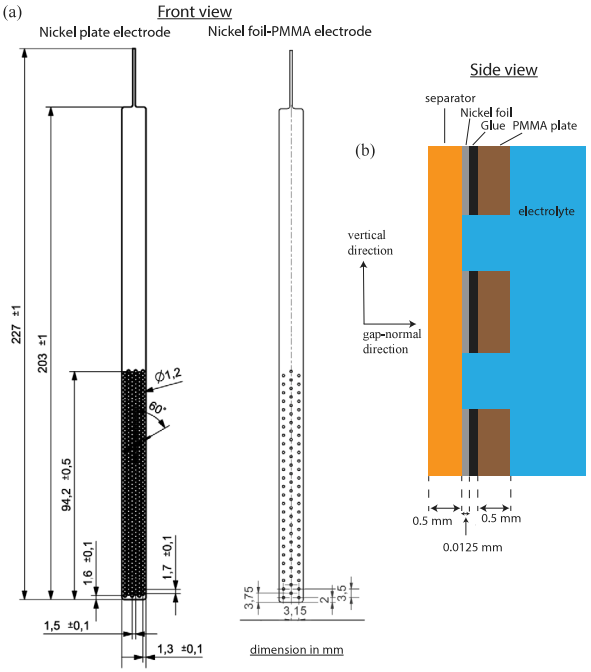

Fig. 10. (a) Dimensions and illustration for porous nickel plate and foil-PMMA electrode at the front view. The distance between the holes for the foil-PMMA electrode is double than that in the plate electrode. (b) Configuration of the assembly of the foil-PMMA electrode at the right-half of the zero gap cell. The assembly for the whole cell is approximately symmetric about the center of the separator.

Moreover, $E_{gap,bub}$ also increases with increasing l_{gap} following Eq. (2) as $\overline{\langle \alpha_{i,gap} \rangle}$ is nearly insensitive to the gap size (except for $\overline{\langle \alpha_{O2,gap} \rangle}$ when $j \geq 0.48$ A/cm^2, see Fig. 9). Therefore, the effect of bubbles to the cell voltage becomes more prominent at higher current densities and larger gap sizes. The largest contribution (0.2 V) as shown in Fig. 9 corresponds to 6% of the total cell voltage shown in Fig. 8.

3.4. Bubbly flow at high current density and cross-separator liquid transport

A crossing behavior of the bulk void fraction has been observed at relatively high current densities as shown in Fig. 5. The void fraction at the O_2 compartment (both at the gap and the bulk) increases over time while that at the H_2 compartment decreases over time, resulting in a much higher void fraction at the O_2 compartment than at the H_2 compartment. However, this behavior does not occur when we change the electrodes from porous nickel plate to nickel-foil supported by a PMMA plate (see the dimensions in Fig. 10). Fig. 11 compares the void fraction profiles measured from experiments using these two types of electrodes. The comparison gives two key findings: 1) bigger bubbles are formed with foil-PMMA electrodes, resulting in larger fluctuations of the mean void fraction, 2) the cross behavior at high current densities in the case with porous plate electrodes is absent in the case of the foil-PMMA electrodes. We refer to the movies of the radiography in the Supplementary data.

We believe these observations can be explained by difference of physical properties of these two electrode types, as listed in Table 1. First nickle plate/foil and PMMA have different wettabilities (note that in foil-PMMA configuration it is the nickel foil facing the membrane and PMMA facing the bulk side). As for the contact angle shown in Table 1, the PMMA surface is less hydrophilic as compared to the nickel surface. This wettability difference well explains the bigger bubbles formed at the foil-PMMA electrode surface as seen in Fig. 11. Apart from that, the pressure between the diaphragm and the electrode for the foil case is higher than the electrode case due to the practicality of the assembly (stronger tightening force needed to keep the cell liquid tight).

Secondly, the foil-PMMA electrode has a much lower porosity (~ 0.1) as compared to the nickel pate electrode (0.5). We think this less porous structure reduces the electrolyte and dissolved gas crossover phenomenon, thus prevents the crossing of the void fraction curves as observed in Fig. 5. To confirm, we try to quantify the liquid crossover by examining the liquid level changes at both compartments. Denote the change of liquid level at the O_2 side after an electrolysis experiment as Δh_{O2} and that at the H_2 side as Δh_{H2}. The initial liquid levels of the two compartments are nearly the same. The stoichiometry for the chemical reaction of water electrolysis shows that H_2 side consumes double the amount of water produced at the O_2 side. If there is no transport between two compartments, $\Delta h_{O2} > 0$ and $\Delta h_{H2} < 0$, which implies always a positive value of $\Delta h_{O2} - \Delta h_{H2}$. In contrast, a negative $\Delta h_{O2} - \Delta h_{H2}$ implies a net transport of liquid/gas from the O_2 side to the H_2 side, even overcoming the hydrostatic pressure difference.

Fig. 12 shows the results of the liquid level change analysis in a zero-gap cell with nickel porous plate or foil-PMMA electrodes at different current densities. For the porous plate electrode case, $\Delta h_{O2} - \Delta h_{H2} < 0$ is observed (even for other gap sizes in nearly all experiments, though not shown here). This implies a significant liquid transport from the anodic compartment (O_2 side) to the cathodic compartment (H_2 side). The same phenomenon was observed and discussed in previous literature [25,26,31]. They attribute this crossover to the electro-osmotic flow, which is driven by the movement of positive ions (K^+) at the electric-double layer due to the presence of an electric potential difference, and becomes significant when the potential difference is large and the size of the channels is small with high porosity. As the current density increases with potential differences, the electro-osmotic flow becomes stronger with increasing current densities. This is indeed the case as seen in Fig. 12 that the crossover rate is enhanced with increasing current density for a porous nickel plate electrode.

In contrast, for the much less porous foil-PMMA electrode, $\Delta h_{O2} - \Delta h_{H2}$ is found always positive in the figure. This implies a limited liquid transport between two compartments. In addition to the lower porosity, bigger bubbles grow (longer residence time) at the holes on the (PMMA) surface, as explained earlier, which might also explain this transport limit.

To summarize, the analysis of liquid level change in electrolysis experiments clearly reveals an enhanced liquid crossover from the anodic compartment to the cathodic compartment in our (small-size)

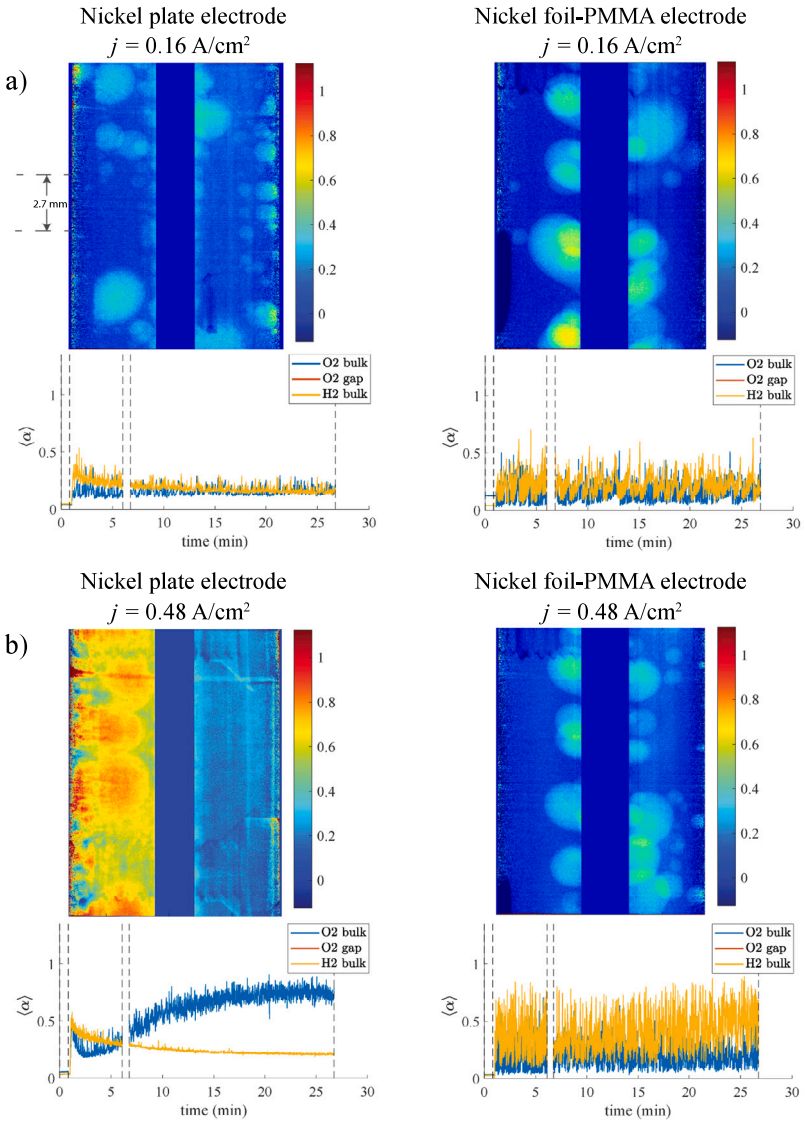

Fig. 11. Spatially averaged void fraction versus time in one set of measurements with two different current densities applied with the radiography snapshot at around 20 min for nickel plate electrode (left) and nickel foil-PMMA electrode (right). The scanning heights are centred at H = 60 mm. Their initial KOH concentrations are both 24 wt% and the gap sizes are zero. See also the videos in the Supplementary data.

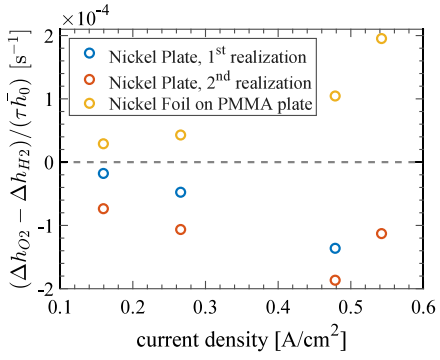

Fig. 12. Change of liquid level at O_2 side Δh_{O2} minus change of liquid level at H_2 side Δh_{H2} after an electrolysis experiment, normalized by the average initial liquid level before any electrolysis experiment $\overline{h_0}$ and the duration of the electrolysis experiment τ. These three sets of experiments are all zero gap with KOH 24 wt%. We note that the liquid level change results might also account for (1) small loss of liquid via splashing out at the top of the cell in particular at high current densities and (2) bubbles remained in the cell before and after the electrolysis experiments. These effects are similar for the same current density, meaning that the comparison between the foil and the plate electrode cases is valid.

cell using a relatively large porous electrode at higher current densities. This might provide a convincing explanation to the cross behavior of the two bulk gas fractions from experiments with the nickel plate electrode, while is was not observed from experiments with the foil-PMMA electrode, as seen in Figs. 5 and 11.

3.4.1. *Effect of the cross-separator liquid flow*

The liquid crossover for the porous plate electrode leads to excess liquid loses/depletion at the anodic compartment, while a constant volumetric flux of gas production is retained. As a result, the measured void fraction from X-ray scanning increases in time, which becomes apparent at higher current densities. In the cathodic compartment, however, the crossover leads to a liquid gain with a constant depletion due to HER, thus resulting in a slightly decreasing void fraction in time. As the crossover is suppressed using the foil-PMMA electrode, the void fraction measured in the two compartments stays rather steady, though with a slow increase in the void fraction in the cathodic compartment due to the faster liquid depletion there.

As discussed in Ref. [26], the presence of such cross-separator flow can lead to undesirable crossover of dissolved oxygen, and this can be suppressed by hydrostatic pressure difference corresponding

to approximately 0.1 m of liquid level difference [25]. Note that we estimate a net velocity of 1.5 μm/s normal to the separator due to this liquid crossover, which is close to the electro-osmotic velocity of 1 μm/s reported in [26], although that was for different molar concentration ($c = 0.1$ M) and current density ($j = 0.126$ A cm^{-2}). The detailed estimation is shown in Appendix C (Supplementary data).

4. Conclusions and outlook

To the best knowledge of the authors, this work for the first time reveals the void fraction distribution in a zero/narrow gap alkaline water electrolyzer using X-ray radiography. With these measurement, we clear up some speculations/hypothesis in the open literature regarding the effect of gas bubbles/film on the cell performance as concluded below. The experiments have been carried out using an in-house built 8.1 mm × 7.8 mm × 198 mm cell with adjustable gap sizes ranging from 0 μm to 300 μm using KOH concentration 24 wt% at different operating current densities varied between 0.01 A/cm^2 and 0.54 A/cm^2, and each current density was applied in constant current mode.

First of all, the measured gas fraction is reported individually at anodic compartment (O_2 side), cathodic compartment (H_2 side), anodic gap, and cathodic gap. The overall void fraction increases with increasing current density. The void fraction at the gaps are found to be rather stable/consistent along the cell height regardless of the gap size. Our measurements do not show evidence on bubble trapping or gas film formation in the gap as suggested in literature. The void fraction at the bulk is found to increase along the cell height, however it was nearly insensitive to the gap size. Interestingly, a crossover behavior of the bulk void fractions, i.e. $\overline{\langle \alpha_{O2} \rangle}$ increasing in time and $\overline{\langle \alpha_{H2} \rangle}$ decreasing in time, is observed with a significantly higher void fraction at the anodic compartment in our experiments at higher current densities. This is a consequence of liquid crossover/transport between the two compartments with an enhancement by high porosity of the electrodes, which is evidenced by the liquid level change comparing cases with electrodes of different porosities.

Furthermore, our voltage measurements imply that a zero gap configuration (within 15 μm resolution) is still most efficient compared to finite small gaps up to 300 μm. Applying the Bruggeman model using the measured gas fraction, the cell potential drop due to the presence of bubbles/gas at the gap is estimated to be maximum 6% of the total cell voltage at $j = 0.54$ A cm^{-2} up to a gap size $l_{gap} = 300$ μm. This finding does not agree with the suggestion e.g. in Ref. [13] of introducing a gap of 200 μm to improve the cell efficiency by allowing easier escape of the bubbles. However, we do stress that the different ways of the cell assembly in our work and in Ref. [13] might result in different compression conditions, which can play an important role in the cell performance and are subject to further investigation.

Moreover, liquid crossover from the O_2 to the H_2 side was observed like in Ref. [26]. In the current study, we found that the crossover was suppressed when the electrode porosity was reduced and a thin film electrode attached to a PMMA surface with lower wettability was applied.

Finally, we have faced quite some challenges in X-ray measurement and data processing, e.g., strong artefacts occurring at the electrodes because of huge scattering of the X-rays due to the high mass density of the electrodes, and complicated correction required during data processing as a consequence of not completely refreshed electrolyte in the experiment series. Future study should address these issues for a refined experimental/measurement design. For example, to maintain the concentration of the electrolyte solution, one can connect the chambers with a pump and a reservoir of electrolyte. To reduce the scattering of X-rays at the electrode, one may employ a thinner and/or less dense electrode. However, finding such a material that is chemically resistant to the electrolyte (KOH) can be challenging, and a thinner electrode can induce higher ohmic heating.

CRediT authorship contribution statement

On-Yu Dung: Writing – original draft, Visualization, Investigation, Formal analysis, Conceptualization. **Stephan Boden:** Writing – review & editing, Visualization, Software, Resources, Methodology, Investigation, Formal analysis, Data curation. **Albertus W. Vreman:** Writing – review & editing, Supervision, Conceptualization. **Niels G. Deen:** Writing – review & editing, Supervision, Project administration. **Markus Schubert:** Writing – review & editing, Resources, Project administration. **Yali Tang:** Writing – review & editing, Supervision, Project administration, Funding acquisition, Conceptualization.

Declaration of generative AI in scientific writing

During the preparation of this work the author(s) used ChatGPT in order to correct the grammar of certain sentences. After using this tool/service, the author(s) reviewed and edited the content as needed and take(s) full responsibility for the content of the publication.

Declaration of competing interest

The authors declare the following financial interests/personal relationships which may be considered as potential competing interests: Y. Tang reports financial support was provided by Dutch Research Council. Y. Tang reports financial support was provided by Nobian. A.W. Vreman reports a relationship with Nobian that includes: employment. If there are other authors, they declare that they have no known competing financial interests or personal relationships that could have appeared to influence the work reported in this paper.

Acknowledgment

This project is funded by NWO (ECCM KICKstart DE-NL program, KICH1.ED04.20.014) and co-funded by Nobian. Hans Lammers (Nobian) is acknowledged for suggesting foil-PMMA electrodes. Jan Timmers and Bart van Sassen are acknowledged for the design of the prototype and the improvement to the final design of the electrolyzer, respectively. We acknowledge the technician Hans van Griensven from the Power and Flow group for giving advices on the design, Henri Vliegen and Thijs van Mol for the mechanical support, and the Eindhoven Prototype Center (EPC) (Gerrit Fimerius, Luciano Oorthuizen, and Bram Kerkhoff) for building the components of the setup. We also acknowledge the technicians Nico Bley, André Flaisz, Jan Schäfer, Ronny Berger, and Uwe Sprewitz at HZDR for the technical support of the X-ray experiments at HZDR. Frank Barthel and Dominic Windisch are also thanked for their patience with us since we occupied and blocked the X-ray laboratory almost all the time. We thank Prof. Uwe Hampel for approval and the facilitation of this project at HZDR.

Appendix A. Supplementary data

Supplementary material related to this article can be found online at https://doi.org/10.1016/j.ijhydene.2025.01.110.

References

[1] IEA. The future of hydrogen. Tech. rep., Paris: IEA; 2019, URL https://www.iea.org/reports/the-future-of-hydrogen.

[2] Phillips R, Dunnill CW. Zero gap alkaline electrolysis cell design for renewable energy storage as hydrogen gas. RSC Adv 2016;6:100643–51. http://dx.doi.org/10.1039/c6ra22242k.

[3] de Groot MT, Vreman AW. Ohmic resistance in zero gap alkaline electrolysis with a zirfon diaphragm. Electrochim Acta 2021;369. http://dx.doi.org/10.1016/j.electacta.2020.137684.

[4] Hreiz R, Abdelouahed L, Fünfschilling D, Lapicque F. Electrogenerated bubbles induced convection in narrow vertical cells: A review. Chem Eng Res Des 2015;100:268–81.

[5] Tjaden B, Cooper SJ, Brett DJL, Kramer D, Shearing PR. On the origin and application of the bruggeman correlation for analysing transport phenomena in electrochemical systems. Curr Opin Chem Eng 2016;12:44–51. http://dx.doi.org/10.1016/j.coche.2016.02.006.
[6] Zarghami A, Deen N, Vreman A. Cfd modeling of multiphase flow in an alkaline water electrolyzer. Chem Eng Sci 2020;227:115926.
[7] Vogt H. On the gas-evolution efficiency of electrodes I–Theoretical. Electrochim Acta 2011;56(3):1409–16.
[8] Vogt H. On the gas-evolution efficiency of electrodes. II–Numerical analysis. Electrochim Acta 2011;56(5):2404–10.
[9] Tobias CW. Effect of gas evolution on current distribution and ohmic resistance in electrolyzers. J Electrochem Soc 1959;106(9):833.
[10] Kienzlen V, Haaf D, Schnurnberger W. Location of hydrogen gas evolution on perforated plate electrodes in zero gap cells. Int J Hydrog Energy 1994;19(9):729–32.
[11] Nagai N, Takeuchi M, Kimura T, Oka T. Existence of optimum space between electrodes on hydrogen production by water electrolysis. Int J Hydrog Energy 2003;28(1):35–41.
[12] Lavorante MJ, Reynoso CY, Franco JI. Water electrolysis with zirfon® as separator and naoh as electrolyte. Desalin Water Treat 2015;56(13):3647–53.
[13] Haverkort J, Rajaei H. Voltage losses in zero-gap alkaline water electrolysis. J Power Sources 2021;497:229864. http://dx.doi.org/10.1016/j.jpowsour.2021.229864.
[14] Bleeker J, van Kasteren C, van Ommen J, Vermaas D. Gas bubble removal from a zero-gap alkaline electrolyser with a pressure swing and why foam electrodes might not be suitable at high current densities. Int J Hydrog Energy 2024;57:1398–407. http://dx.doi.org/10.1016/j.ijhydene.2024.01.147.
[15] Abdelouahed L, Hreiz R, Poncin S, Valentin G, Lapicque F. Hydrodynamics of gas bubbles in the gap of lantern blade electrodes without forced flow of electrolyte: Experiments and cfd modelling. Chem Eng Sci 2014;111:255–65. http://dx.doi.org/10.1016/j.ces.2014.01.028.
[16] Rox H, Bashkavtov A, Yang X, Loos S, Mutschke G, Gerbeth G, et al. Bubble size distribution and electrode coverage at porous nickel electrodes in a novel 3-electrode flow-through cell. Int J Hydrog Energy 2023;48:2892–905. http://dx.doi.org/10.1016/j.ijhydene.2022.10.165.
[17] Riegel H, Mitrovic J, Stephan K. Role of mass transfer on hydrogen evolution in aqueous media. J Appl Electrochem 1998;28:10–7. http://dx.doi.org/10.1023/A:1003285415420.
[18] Yuan S, Zhao C, Cai X, An L, Shen S, Yan X, et al. Bubble evolution and transport in pem water electrolysis: Mechanism, impact, and management. Prog Energy Combust Sci 2023;96:101075. http://dx.doi.org/10.1016/j.pecs.2023.101075.
[19] Jeon DH, Kim S, Kim M, Lee C, Cho H-S. Oxygen bubble transport in a porous transport layer of polymer electrolyte water electrolyzer. J Power Sources 2023;553:232322. http://dx.doi.org/10.1016/j.jpowsour.2022.232322.
[20] Mandalahalli MM, Wagner EC, Portela LM, Mudde RF. Electrolyte effects on recirculating dense bubbly flow: An experimental study using X-ray imaging. AIChE J 2020;66:e16696. http://dx.doi.org/10.1002/aic.16696.
[21] Haug P, Kreitz B, Koj M, Turek T. Process modelling of an alkaline water electrolyzer. Int J Hydrog Energy 2017;42:15689–707. http://dx.doi.org/10.1016/j.ijhydene.2017.05.031.
[22] Hu S, Guo B, Ding S, Yang F, Dang J, Liu B, et al. A comprehensive review of alkaline water electrolysis mathematical modeling. Appl Energy 2022;327. http://dx.doi.org/10.1016/j.apenergy.2022.120099.
[23] de Groot M, Kraakman J, Barros RLG. Optimal operating parameters for advanced water electrolysis. Int J Hydrog Energy 2022;47:34773–83. http://dx.doi.org/10.1016/j.ijhydene.2022.08.075.
[24] Barros RLG, Kraakman JT, Sebregts C, van der Schaaf J, de Groot MT. Impact of an electrode-diaphragm gap on diffusive hydrogen crossover in alkaline water electrolysis. Int J Hydrog Energy 2024;49:886–96. http://dx.doi.org/10.1016/j.ijhydene.2023.09.280.
[25] Haverkort JW. Modeling and experiments of binary electrolytes in the presence of diffusion, migration, and electro-osmotic flow. Phys Rev Appl 2020;14. http://dx.doi.org/10.1103/PhysRevApplied.14.044047.
[26] Haverkort JW, Rajaei H. Electro-osmotic flow and the limiting current in alkaline water electrolysis. J Power Sources Adv 2020;6:100034. http://dx.doi.org/10.1016/j.powera.2020.100034.
[27] Agfa-Gevaert N. Technical data sheet: Zirfon perl utp 500. 2020.
[28] Porombka P, Boden S, Lucas D, Hampel U. Horizontal annular flow through orifice studied by X-ray microtomography. Exp Fluids 2021;62. http://dx.doi.org/10.1007/s00348-020-03091-6.
[29] Ma Y, Cao X, Feng X, Ma Y, Zou H. Fabrication of super-hydrophobic film from pmma with intrinsic water contact angle below 90°. Polymer 2007;48(26):7455–60. http://dx.doi.org/10.1016/j.polymer.2007.10.038.
[30] Horsthemke A, Schröder JJ. The wettability of industrial surfaces: Contact angle measurements and thermodynamic analysis. Chem Eng Process Process Intensif 1985;19(5):277–85. http://dx.doi.org/10.1016/0255-2701(85)80020-9.
[31] Gennes P-G, Brochard-Wyart F, Quéré D, et al. Capillarity and wetting phenomena: drops, bubbles, pearls, waves. Springer; 2004.